https://doi.org/10.1016/j.apenergy.2021.117357
This is the Pre-Published Version.

Optimization of gas diffusion layer in high temperature PEMFC with the focuses on thickness and porosity

Lingchao Xia [a], Meng Ni [a, *], Qijiao He [a], Qidong Xu [a], Chun Cheng [a]

[a] *Building Energy Research Group, Department of Building and Real Estate, Research Institute for Sustainable Urban Development (RISUD), The Hong Kong Polytechnic University, Hung Hom, Kowloon, Hong Kong, China*

Corresponding author: Email – meng.ni@polyu.edu.hk (M.Ni); Tel: 852-27664152

Abstract:

Wide ranges of thickness (e.g. 100-400 μm) and porosity (e.g. 30-70%) of gas diffusion layer (GDL) in a high temperature proton exchange membrane fuel cell (HT-PEMFC) are available in the literature. However, the effects of GDL porosity and thickness on electron conduction and gas distribution uniformity (under the rib and under the channel) are unclear. In this study, a numerical non-isothermal 3D model was developed. After model validation, parametric analyses were performed to investigate the effects of thickness and porosity on flow uniformity (under the rib and under the channel), diffusion flux and ohmic resistance. It is found that both the flow uniformity and ohmic resistance increase with increasing thickness and porosity. However, the thickness and porosity have opposite influence on diffusion flux, which decreases with increasing GDL thickness but increases with increasing porosity. Unlike the previous research suggesting thin GDL with high porosity, optimal GDL thickness and porosity are found in the present study. The appropriate GDL thicknesses for anode and cathode are 80-120 μm and 140-170 μm respectively while the optimal value for GDL porosity is 35-45%. This study clearly demonstrates that we can further achieve a performance increment of

© 2021. This manuscript version is made available under the CC-BY-NC-ND 4.0 license https://creativecommons.org/licenses/by-nc-nd/4.0/

7.7% by carefully controlling the thickness and porosity of GDL.

Key words: HT-PEMFC; Gas diffusion layer; Geometric optimization; Porosity; Flow uniformity.

Nomenclature

E	Ideal voltage [V]	η_{ohmic}	Ohmic loss [V]
E^0	Open circuit voltage [V]	η_{conc}	Concentration loss [V]
E_a	Activation energy [J/mol]	η_{act}	Activation loss [V]
T	Operating temperature [°C]	R_{ohmic}	Ohmic resistance [ohm]
$a_{pro}^{v_i}$	Product pressure [Pa]	R_{elec}	Electron resistance [ohm]
$a_{rea}^{v_i}$	Reactant pressure [Pa]	R_{ionic}	Ionic resistance [ohm]
R	Universal gas constant [J/mol/K]	n	Moles [mol]
F	Faraday constant [C/mol]	c_R^0	Reactant concentration in GDL [mol/m^3]
j_0	Exchange current density [A/cm^2]	c_R^*	Reactant concentration in CL [mol/m^3]
j	Current density [A/cm^2]	α	Charge transfer coefficient
i	Current [A]	DL	Doping level of H_3PO_4
u	Velocity [m/s]	ρ	Density [kg/m^3]
Q	Heat generation [W/m^3]	μ	Dynamic viscosity [kg/m·s]
k	Thermal conductivity [W/m·K]	C_p	Heat capacity [J/mol·K]
Pt/C	Platinum to carbon ratio	R_{pt}	Surface area per unit mass [m^2/g]

1. Introduction

1.1 Background

High temperature proton exchange membrane fuel cell (HT-PEMFC) is a promising alternative of clean power resources which can convert the chemical energy into electricity directly. It overcomes the water flooding issue in low temperature PEMFC (LT-PEMFC) with simplified water management [1-3], higher CO tolerance [4-9] and enhanced reaction kinetics [10, 11] by raising the working temperature to the range of 120-200 °C.

Among all the components of HT-PEMFC, the investigation on membrane [12-14], catalyst layer [15-17] and flow field design [18-20] have attracted lots of attention while little research has been conducted on gas diffusion layer (GDL) in HT-PEMFC. However, GDL plays an important role in mass transport, heat transfer and electron conduction. Thus, the research on GDL in HT-PEMFC is highly needed. It should be noted that although much research has been conducted on GDL in LT-PEMFC, it remains necessary to perform a comprehensive study to reveal the GDLs' effect as the conclusions from the LT-PEMFC cannot be directly adopted in HT-PEMFC due to the significantly different mass transport. In LT-PEMFCs, the liquid-gas two-phase flow inside the cell [21-23] and droplet dynamics at GDL surface [24] must be carefully considered since the operating temperature is below 100 ºC. In HT-PEMFC, water molecules exist in the form of gas. The mass transport, temperature distribution and electrochemical behaviors of HT-PEMFC and LT-PEMFC can greatly differ.

The important properties of GDL include geometric parameters (Length/Width/Thickness), porosity, electrical conductivity, thermal conductivity, and heat capacity. Generally, the electrical conductivity, thermal conductivity, and heat capacity are constants for a specific

material. Besides, the current density of fuel cell gets normalized in length and width, leaving thickness and porosity to be selected for further investigation.

By now, the reported thickness of GDL in HT-PEMFC ranges from 100 μm to 490 μm [25-27]. The commercial GDL varies in the range of thickness with different brands such as ELAT (406-490 μm), JNT(200-350μm) and Toray (110-370 μm) [28]. Zhang et al. [29] reported that the mechanical behavior is not sensitive to the GDL thickness due to the negligible effect of different thickness (190 μm, 280 μm, 370 μm selected) on stress-strain curves. Thus, thickness effect on mechanical support can be neglected in the present study. Tawfiq et al. [30] reported that cell performance would be improved with a lower thickness of GDL. However, the limited range 300-420 μm was adopted in their work while the effect of GDL thickness on cell performance might differ with a thinner GDL such as 50-150 μm. Since GDL is used to support gas diffusion, is the GDL thickness the thinner the better?

For the GDL porosity, the popular commercial GDLs' porosity ranges from 31.8% to 73.9% [27]. It is believed that this range can be further narrowed to guide the manufacture of GDL and improve cell performance. Tawfiq et al. [30] conducted an investigation of GDL porosity and reported that higher porosity would lead to a better cell performance. This phenomenon was further confirmed by Jha et al. [31]. Firstly, three values of porosity (17%, 20%, 40%) were adopted in Tawfiq's work. Then this porosity range was increased to 20-60% by Jha et al. [31] and they reported that the GDL porosity should be the higher the better in their studied range. However, in their study, the effect of GDL porosity on the electron conduction was not considered. It could be expected that a high GDL porosity might decrease the effective conductivity of GDL. Thus, whether the GDL porosity should be the higher the better needs to

be re-evaluated.

1.2 Research gap

The previous studies on HT-PEMFC suggest that the GDL should be the thinner the better and the GDL porosity should be the higher the better. However, for practical HT-PEMFC, interconnectors are used to electrically connect multiple cells to deliver a high power and a high voltage. The existence of interconnector ribs may cause the reactant concentration in the catalyst layer (CL) to be much lower under the ribs than under the channels. What is the effect of GDL thickness on the reactants' distribution uniformity in the CL? Is the GDL thickness the thinner the better? Can a thicker GDL help improve the reactants' distribution uniformity? Are there any optimal GDL thickness?

In the previous research, the effect of GDL porosity on electron conduction was not considered, leading to a conclusion that the GDL porosity should be the higher the better. As the GDL porosity would affect the effective conductivity of the GDL, a too high porosity may cause a high ohmic loss due to a low effective conductivity. Thus, the previous conclusion on GDL porosity might not be valid.

1.3 New contributions

As discussed above, the main limitations of the previous works are: (1) the effects of GDL thickness and porosity on the reactants' distribution uniformity (under the channel and under the rib) are not considered; and (2) the effect of GDL porosity on the electron conduction through GDL is not considered. To address the scientific questions and issues mentioned above, this work aims to provide a comprehensive understanding of GDL's effects on HT-PEMFC, especially the effects of GDL thickness and porosity. In this work, a numerical non-isothermal

three-channel 3D model was developed. There are 3 new features of this study: (1) simulations are conducted under much wider ranges of GDL thickness (20-380 μm) and porosity (0-100%); (2) for the first time, the comprehensive effects of thickness and porosity on flow uniformity (especially gas distribution in the catalyst layer under the rib and under the channel) are fully considered; and (3) the effect of GDL porosity on the effective conductivity is considered. Therefore, the present study fully considers the effects of GDL on gas distribution uniformity, diffusion flux and electron conduction.

The new contributions of this work include: (1) providing in-depth understanding on the effects of thickness and porosity of GDL on the gas distribution uniformity, diffusion flux, and electron conduction; (2) identifying optimal GDL thicknesses and GDL porosity for the anode and cathode for improving the performance of HT-PEMFC. Based on the present study, it is clearly shown that 7.7% performance enhancement of HT-PEMFC can be achieved by carefully controlling the thickness and porosity of GDL.

2. Model development

2.1 Computational domain and assumptions

Fig. 1 shows the schematic of computational domain of HT-PEMFC, which includes two bipolar plates (BPs), two gas channels, two gas diffusion layers (GDLs), two catalyst layers (CLs) and one proton exchange membrane (PEM). Oxygen reduction reaction (ORR) and hydrogen oxidation reaction (HOR) occurs inside the two CLs, respectively.

$$\begin{aligned} &\text{Cathode}: \quad \frac{1}{2}O_2 + 2H^+ + 2e^- \rightarrow H_2O \\ &\text{Anode}: \quad\quad H_2 \rightarrow 2H^+ + 2e^- \end{aligned} \tag{1}$$

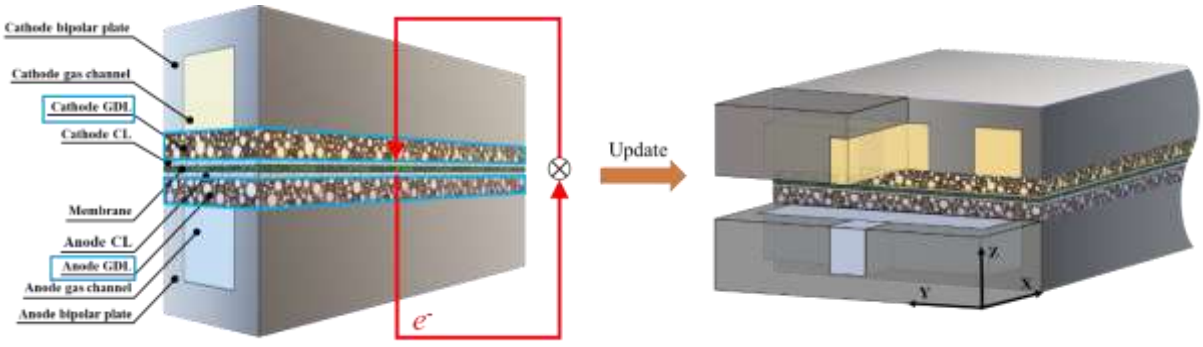

Fig. 1. Schematic of computational domain for one unit cell

Comparing the model developed in this work with the previous research, the single channel model was updated with a three-channel model. To distinguish these three channels with each other, a chamber, and a shell with one gas inlet was adopted for both electrodes. The coordinate system is as shown in Fig. 1.

2.2 Governing equations

2.2.1 Electrochemistry

The generated current can be calculated by the Butler-Volmer equations (2 & 3).

$$i_a = i_{0,a}\left(\frac{C_{H_2}}{C_{H_{2,ref}}}\right)^{0.5}\left(e^{\frac{n\alpha_a F}{RT}\eta_a} - e^{\frac{-n(1-\alpha_a)F}{RT}\eta_a}\right) \quad (2)$$

$$i_c = i_{0,c}\left(\frac{C_{O_2}}{C_{O_{2,ref}}}\right)^{1}\left(-e^{\frac{n(1-\alpha_c)F}{RT}\eta_c} + e^{\frac{-n\alpha_c F}{RT}\eta_c}\right) \quad (3)$$

where C represents the concentration of reactants, R is universal gas constant, T is the working temperature, α is the transfer coefficient and $i_{o,a/c}$ is the exchange current density governed by equation (4):

$$i_{0,a/c} = A_v \bullet i_{0,a/c\_ref} \quad (4)$$

where A_v is catalyst layer's specific surface area (m^2/m^3), i_{0,a_ref} and i_{0,c_ref} are reference exchange current density at anode and cathode catalyst layer (A/m^2), respectively. The reference exchange current density is calculated by equation (5 & 6) [32]:

$$i_{0,a\_ref} = 7.135\exp[-1400(1/T - 1/353.15)] \quad (5)$$

$$i_{0,c\_ref} = 1.2286\text{e-}6\exp[-7900(1/T - 1/353.15)] \quad (6)$$

$\eta_{a,c}$ in equation (2 & 3) represents the activation loss and can be calculated by equation (7 & 8):

$$\eta_a = \phi_s^a - \phi_l^a - E_{eq}^a \quad (7)$$

$$\eta_c = \phi_s^c - \phi_l^c - E_{eq}^c \quad (8)$$

where ϕ represents the electric potential (V) and E_{eq} represents the equilibrium electric potential. The potential values at two electrodes are governed by equation (9):

$$E_{eq}^a = 0; \quad E_{eq}^c = E_{Nernst} \quad (9)$$

Membrane conductivity is dependent on the local temperature and doping level of phosphoric acid, as shown in equation (10):

$$\sigma_{mem} = \sigma_0 \exp[\tfrac{-619.6DL+21750}{R}(-1/T + 1/453.15)] \quad (10)$$

where σ_0 represents the conductivity (S/m) under the condition of 180 °C and the value of DL is set as 5 based on reference [14]. Correction of conductivity within porous media in CLs is governed by Bruggeman equation (11):

$$\sigma_{l/s,CL} = \varepsilon_{l/c}^{1.5}\sigma_{l/s} \quad (11)$$

where ε represents the porosity (%).

2.2.2 Flow field and mass transport

The momentum transfer of the laminar gas flow in gas channel is governed by equation (12):

$$\rho(\vec{v}\bullet\nabla\vec{v}) = \nabla\left\{-p\mathbf{I} + \mu[\nabla\vec{v} + (\nabla\vec{v})^T]\right\} \quad (12)$$

where ρ represents the density, v represents the velocity and μ represents the dynamic viscosity.

The mass transport is governed by equation (13):

$$\nabla\left\{-\rho w_i\sum_{j=1}^{N}D_{ij}[\frac{M}{M_j}\left(\nabla w_j+w_j\frac{\nabla M}{M}\right)+\left(x_j-w_j\right)\frac{\nabla P}{P}]+w_i\rho\vec{v}\right\}=R_i \qquad (13)$$

where D represents the binary diffusion coefficient (m^2/s) and the molar fraction of nitrogen in the cathode can be calculated by equation (14):

$$w_{N_2}=1-w_{O_2}-w_{H_2O} \qquad (14)$$

The gas velocity in both anode and cathode are governed by equation (15 & 16) respectively taking consideration of the stoichiometric (St) number λ, molar fraction w (%), and temperature T:

$$U_{in\_cathode}=\lambda_c\frac{I}{4F}w_{O_2}RT/(p\bullet A_{channel}) \qquad (15)$$

$$U_{in\_anode}=\lambda_a\frac{I}{2F}w_{H_2}RT/(p\bullet A_{channel}) \qquad (16)$$

The dynamic viscosity of each specie under different temperature can be calculated by expressions summarized in Table 1. The multicomponent dynamic viscosity and density of gas mixture can be calculated by equation (17& 18):

$$\mu_{a,c}=\sum_{i=1}^{n}\frac{w_i\mu_i}{\sum_{j=1}^{n}(w_j\sqrt{\frac{M_j}{M_i}})} \qquad (17)$$

$$\rho=\mathrm{p(RT}\sum_i\frac{w_i}{M_i})^{-1} \qquad (18)$$

Table 1 Mass transport and thermal properties [33]

Parameters	Value
Dynamic viscosity of H_2	(27.758+2.12E-1*T-3.28E-5*T*T) *1e-7 [Pa·s]
Dynamic viscosity of N_2	(42.606+4.75E-1*T-9.88E-5*T*T) *1e-7 [Pa·s]
Dynamic viscosity of O_2	(44.224+5.62E-1*T-1.13E-5*T*T) *1e-7 [Pa·s]
Dynamic viscosity of H_2O	(-36.826+4.29E-1*T-1.62E-5*T*T) *1e-7 [Pa·s]

Heat capacities of H_2	25.40+2.0178E-2*T-3.8549E-5*T^2+3.1880E-8*T^3-8.7585E-12*T^4 [J/mol·K]
Heat capacities of N_2	29.34-3.5395E-3*T+1.0076E-5*T^2-4.3116E-9*T^3+2.5935E-13*T^4 [J/mol·K]
Heat capacities of O_2	29.53-8.8999E-3*T+3.8083E-5*T^2-3.2629E-8*T^3+8.8607E-12*T^4 [J/mol·K]
Heat capacities of H_2O	33.93-8.4186E-3*T+2.9906E-5*T^2-1.7825E-8*T^3+3.6934E-12*T^4 [J/mol·K]
Thermal conductivities of H_2	0.03591+4.5918E-4*T-6.4933E-8*T^2 [W/m/K]
Thermal conductivities of N_2	0.00309+7.5930E-5*T-1.1014E-8*T^2 [W/m/K]
Thermal conductivities of O_2	0.00121+8.6157E-5*T-1.3346E-8*T^2 [W/m/K]
Thermal conductivities of H_2O	0.00053+4.7093E-5*T+4.9551E-8*T^2 [W/m/K]
Diffusion coefficient D_{H2H2O}	$9.15\times10^{-5}\times\left(\frac{T}{307.1}\right)^{1.75}\left[m^2/s\right]$
Diffusion coefficient D_{N2H2O}	$2.56\times10^{-5}\times\left(\frac{T}{307.15}\right)^{1.75}\left[m^2/s\right]$
Diffusion coefficient D_{O2N2}	$2.2\times10^{-5}\times\left(\frac{T}{293.2}\right)^{1.75}\left[m^2/s\right]$
Diffusion coefficient D_{O2H2O}	$2.82\times10^{-5}\times\left(\frac{T}{308.1}\right)^{1.75}\left[m^2/s\right]$

2.2.3 Heat transfer

Generated heat Q by two electrochemical half-reactions at anode and cathode can be calculated by equation (19):

$$Q_{\text{react\_a/c}} = (-T\Delta S_{a/c})\cdot\frac{I}{nF} \tag{19}$$

where $\triangle S_a$ and $\triangle S_c$ represents the entropy change of ORR and HOR ($J\cdot K^{-1}\cdot mol^{-1}$), respectively. Table 2 lists the absolute entropy of each specie. Thus, $\triangle S_a$ and $\triangle S_c$ can be calculated by equations 20 and 21:

$$\Delta S_a = 2S°[H^+(g)] + 2S°[e^-(g)] - S°[H_2(g)] \quad (20)$$

$$\Delta S_c = S°[H_2O(g)] - 2S°[e^-(g)] - 2S°[2H^+(g)] - \frac{1}{2}S°[O_2(g)] \quad (21)$$

Inside CL, the local heat generation by ohmic loss can be calculated by equation (22):

$$Q_{oh} = \left\|\nabla \varphi_{ele}\right\|^2 \sigma_{ele}^{eff} + \left\|\nabla \varphi_{pro}\right\|^2 \sigma_{pro}^{eff} \quad (22)$$

where φ_{ele} and φ_{pro} represent the local potentials of electrode and electrolyte materials in the catalyst layer, σ_{ele} and σ_{pro} represent the conductivity of electron and proton. σ^{eff} represents the effective conductivity with due consideration of porosity. The Activation loss can be calculated by equation (23):

$$Q_{act\_a/c} = j_{a/c} \left| \eta_{act\_a/c} \right| \quad (23)$$

Thus, the total heat generation can be calculated by equation (24):

$$Q_{total} = Q_{react} + Q_{oh} + Q_{act} \quad (24)$$

Heat transfer is governed by the energy equation (25):

$$\nabla \cdot (\rho C_p \vec{v} T) = \nabla \cdot (k \nabla T) + S_T \quad (25)$$

where k represents thermal conductivity, S_T represents the heat source and C_p represents heat capacity of gas mixtures. The multicomponent gas mixture's heat capacity and conductivity can be calculated by equations 26 and 27:

$$C_p = \sum_i w_i (C_p)_i \quad (26)$$

$$k = \sum_i Y_i k_i \quad (27)$$

where Y_i represents mass fraction of each specie (%). More properties and operating conditions are listed in Table 3.

Table 2 Absolute entropy of each specie [34]

Temperature [K]	H_2 [J·K^{-1}·mol^{-1}]	O_2 [J·K^{-1}·mol^{-1}]	H^+ [J·K^{-1}·mol^{-1}]	e^- [J·K^{-1}·mol^{-1}]	H_2O [J·K^{-1}·mol^{-1}]

298.15	130.68	205.157	108.946	20.979	188.834
300	130.858	205.329	109.075	21.107	189.042
350	135.315	209.88	112.279	24.311	/
400	139.216	213.871	115.055	27.087	198.788
450	142.656	217.445	117.503	29.535	/
500	145.737	220.693	119.693	31.725	206.634

Table 3 Physical/chemical properties and operating conditions [35]

Parameters	Value
Channel length	20 [mm]
Channel height	1 [mm]
Channel width	0.7874 [mm]
Rib height	1 [mm]
Rib width	0.9093 [mm]
GDL thickness	0.38 [mm]
CL thickness	0.05 [mm]
Membrane thickness	0.1 [mm]
Bipolar plate thickness	0.5 [mm]
Humidified temperature, T_H	28 [°C]
Working temperature, T_w	180 [°C]
GDL porosity, ε_{GDL}	0.4
GDL permeability, K_{GDL}	1.18e-12 [m^2]
CL porosity, ε_{CL}	0.4
CL permeability, K_{CL}	K_{GDL} /5 [m^2]
Anode stoichiometry number, λ_a	1.2
Cathode stoichiometry number, λ_c	2.0
Molar fraction of H_2, w_{H2}	0.963
Molar fraction of H_2O, w_{H2O}	0.037
Molar fraction of O_2, w_{O2}	0.202
Molar mass of H_2, M_{H2}	2 [g/mol]
Molar mass of N_2, M_{N2}	28 [g/mol]
Molar mass of H_2O, M_{H2O}	18 [g/mol]
Molar mass of O_2, M_{O2}	32 [g/mol]
Anode charge transfer coefficient, α_a	0.5
Cathode charge transfer coefficient, α_c	0.25
Electrolyte conductivity at 180°C, σ_0	9.825 [S/m]
Electrode conductivity, σ_s	222 [S/m]
Bipolar plate conductivity, σ_b	20,000 [S/m]
Reference pressure, P_r	1 [atm]
Ratio of Pt to C, Pt/C	0.3
Specific surface area, A_v	1.05E7 [m^2/m^3]

2.3 Boundary conditions

Detailed boundary conditions are listed in Table 4. Membrane was set as impermeable to all gases. Both anode and cathode back pressures were 1 atm. Hydrogen and air were all humidified under the temperature of 28 °C. The surface of cathode BP is connected to the ground and working voltage was applied to the surface of anode BP. All internal surfaces were no-slip. As a repeating unit cell in a large fuel cell stack was considered in this work, it's reasonable to assume that each unit cell shares the same identical cell behavior. Thus, no heat transfer occurs between each unit cell. In this work, the surface of BPs is adiabatic. The generated heat can only be taken out by gas flow. The interface between GDL and BP is in full contact and compression is neglected in this study.

Table 4 Source terms of species transport

Location	Source term	Unit
Anode	$S_m = S_{H_2} + S_{H_2O}$	Kg/m^{3}s
Cathode	$S_m = S_{O_2} + S_{N_2} + S_{H_2O}$	Kg/m^{3}s
GDL	$S_u = -\frac{\mu}{K}\vec{u}$	Kg/m^{2}s^2
ACL	$S_{H_2} = -\frac{j_a}{2F} M_{H_2}$	Kg/m^{3}s
	$S_{ele} = -j_a$, $S_{ion} = j_a$	A/m^3
CCL	$S_{O_2} = -\frac{j_a}{4F} M_{O_2}$, $S_{H_2O} = \frac{j_a}{2F} M_{H_2O}$	Kg/m^{3}s
	$S_{ele} = j_c$, $S_{ion} = -j_c$	A/m^3

2.4. Numerical method

This three-dimensional non-isothermal model consists of 4 modules including electrochemical module, fluid flow module, mass transfer module and heat transfer module. It

was solved with the finite element method. Parameters adopted in this model are listed in Table 3. To numerically calculate the cell performance, parametric sweep was used with the cathode boundary potential varying from 0.9 V to 0.4 V. The potential interval was 0.1 V. To investigate the effect of GDL thickness and porosity, correspondent parametric sweeps were performed. GDL thickness varies from 20 μm to 380 μm with thickness interval of 20 μm while the GDL porosity varies from 5% to 95% with porosity interval of 5%. The computation work was conducted on a personal computer with Intel Core i7-10700 2.90GHz processor and 16.0 GB RAM. The simulation results converged within 200 iterations and took around 240 minutes for each case.

3. Results and analysis

3.1 Model validation

Grid independence analysis was performed as shown in Fig. 2 (output voltage V_{cell} = 0.5 V). The results show that when the meshing elements is increased from 6,036 to 76,722, the current density significantly decreases from 0.833 A/cm^2 to 0.738 A/cm^2. Then the current density approaches to a constant value with the further increase of meshing elements. As expected, the solution time is found to increase almost linearly with increasing number of meshing elements. Increasing the meshing elements from 76,722 to 109,756 only improves the accuracy by 0.4% but the solution time is almost doubled. Thus, taking consideration of both results accuracy and solution time, the number of meshing elements 76,722 was adopted.

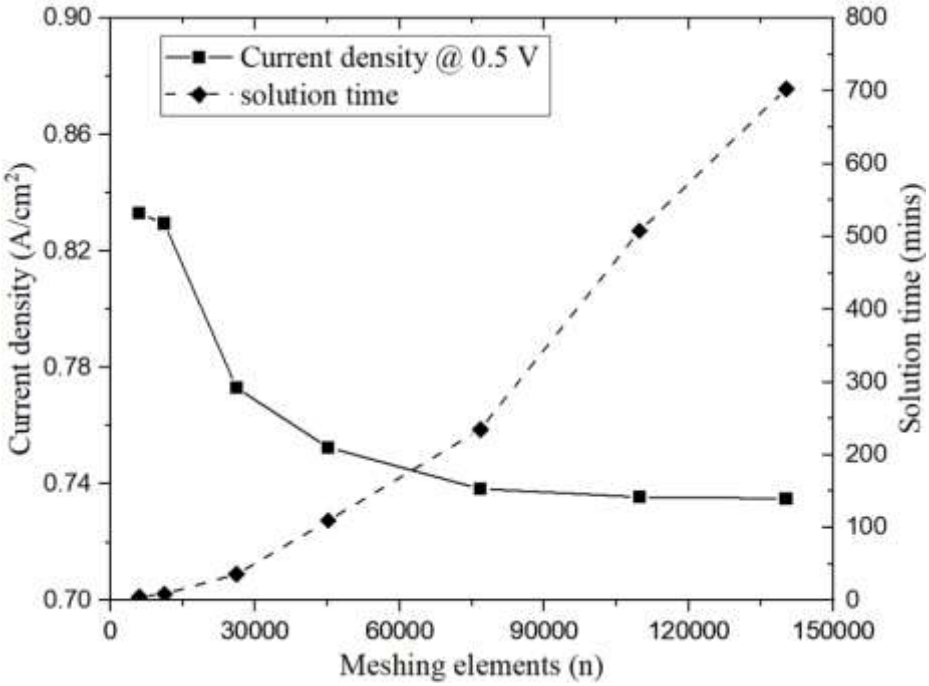

Fig. 2. Grid independence analysis

Preliminary simulation was conducted and compared with the experiment data [35] as shown in Fig. 3. Operation conditions were consistent with the experimental values. The working temperature was 180 °C with humidified hydrogen and air at atmospheric pressure. Stoichiometry numbers were 1.2 and 2 for anode and cathode, respectively. Fig. 3 shows a good agreement between the simulation results and experimental data. It should be noted that for model validation, the thicknesses of GDL for anode and cathode were both 380 μm and GDL porosity was 40%.

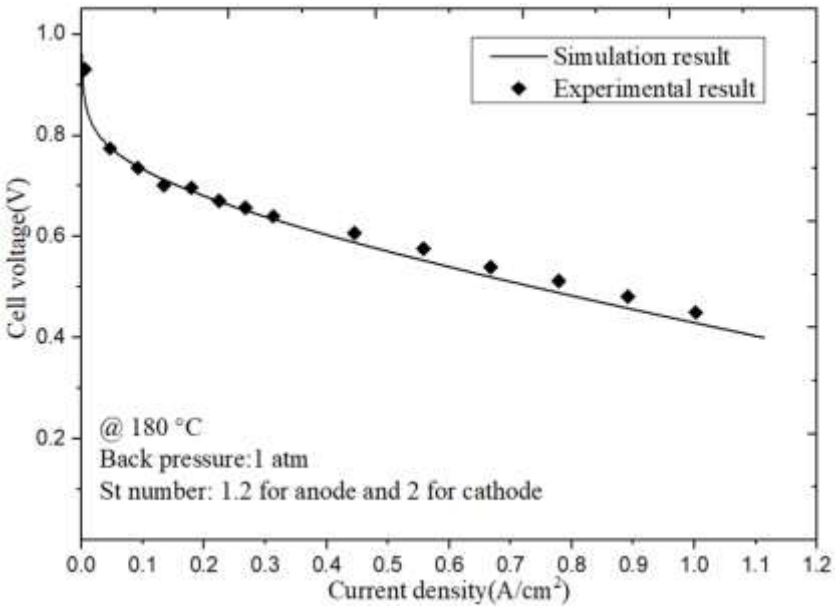

Fig. 3. Comparison between simulation results and experimental data

3.2 Effect of GDLs' thickness

3.2.1 Thickness effect on flow uniformity

The GDL thickness could affect not only gas diffusion along the electrode depth, but also gas distribution under the rib and under the channel. To evaluate the effects of GDL thickness on gas diffusion and gas distribution uniformity, variation of reactants concentration distribution with different GDL thicknesses is shown in Fig. 4. When changing anode or cathode GDL thickness individually, the GDL thickness of the other side remains 380 μm. In Fig. 4(a) with an anode GDL thickness of 20 μm, slightly lower hydrogen concentration under the rib than that under the channel was observed. This uneven gas distribution is more remarkable in the cathode, as the oxygen concentration under the rib is substantially lower than that under the channel (Fig. 4b). With a cathode GDL thickness of 20 μm, the oxygen concentration could even be reduced to zero, which is unacceptable in the operation of fuel cell. One interesting finding of this study is that the gas distribution uniformity can be significantly improved with increasing GDL thickness, especially at the cathode side. This finding means

that the GDL thickness should not be too small, although a thin GDL reduces the concentration overpotential and ohmic loss.

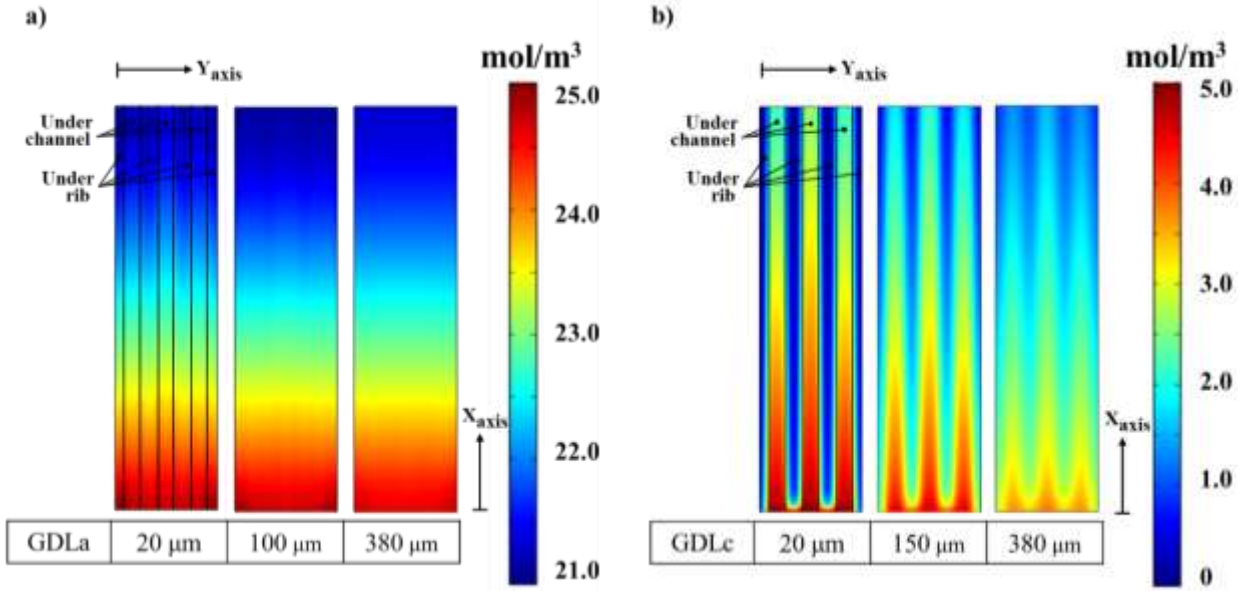

Fig. 4. Concentration distribution of both hydrogen (a) and oxygen (b) in the catalyst layer at 0.4 V, and with various values of GDL thickness

To quantify this effect of GDL thickness on gas distribution uniformity, a standard index γ representing the flow uniformity by Weltens [36] was adopted for analysis as shown in equation (28):

$$\gamma = 1 - \frac{1}{2n} \sum_{n=1}^{n} \frac{\sqrt{(c_n - \bar{c})^2}}{\bar{c}} \tag{28}$$

Detailed results calculated by this equation are shown in Fig. 5, which shows the flow uniformity of reactants transport along the flow direction in Fig. 4.

It is found that the hydrogen distribution in the anode is very uniform while the distribution of oxygen in the cathode is highly uneven. Along the flow direction (X axis), the hydrogen flow uniformity almost remains unchanged (Fig. 5). However, a significant decrease of oxygen flow uniformity is be observed along the flow direction due to the oxygen consumption by

ORR and the large difference in oxygen concentration under the rib and under the channel. This decreasing effect becomes more significant with a thinner cathode GDL. The mean value of the flow uniformity along the channel is extracted, thus the curves indicating the change of flow uniformity with different GDL thicknesses can be obtained (black curves in Fig. 6). At the anode, the hydrogen flow uniformity is slightly increased when the anode GDL thickness increases from 20 to 100 μm (See Fig. 6(a)). Then, the flow uniformity approaches to a constant value with the anode GDL thickness is further increased. By contrast, the oxygen flow uniformity increases significantly with increasing cathode GDL thickness (Fig. 6(b)).

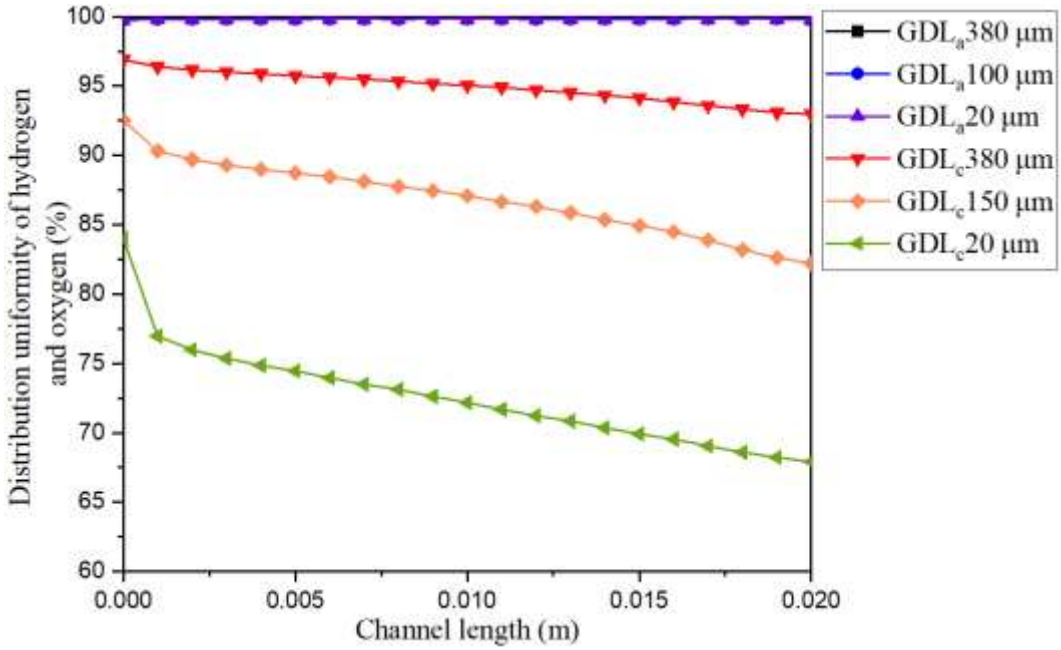

Fig. 5. Gas distribution uniformity of mass transport in CL of both anode and cathode

3.2.2 Thickness effect on diffusion flux

GDL not only helps improve the reactants flow uniformity, but also plays a vital role in mass transfer along the depth of the electrodes (Z direction). To identify this effect of GDL thickness, another standard index named diffusion flux J was adopted governed by the Fick's law:

$$J \equiv \frac{dm}{Adt} = D\frac{\partial C}{\partial Z} \tag{29}$$

where D represents the diffusion coefficient, ∂C represents concentration gradient and ∂Z represents distance gradient. To adjust this equation to this model, it can be corrected as equation (30):

$$J = D\frac{C_{\text{channel}} - C_{CL}}{\delta_{GDL}} \tag{30}$$

where $C_{channel,CL}$ represent the concentration in the gas channel and CL, δ_{GDL} represents GDL thickness. Since the diffusion coefficient is independent of the geometric parameters of GDL, $C_{channel}$ and C_{CL} are based on the primary value of cell operation, the diffusion flux would be directly affected by the GDL thickness δ_{GDL}. The variation of diffusion flux with different anode and cathode GDL thicknesses are shown as red curves in Fig. 6. The results reveal that the diffusion flux has an inversely proportional relationship with GDL thickness. The anode diffusion flux is almost 60 mol/(m^2s) with anode GDL thickness to be 20 μm while the maximum cathode diffusion flux is only 3 mol/(m^2s). This big difference is attributed by the large difference in diffusion coefficient of hydrogen and oxygen. To conclude, the decline of diffusion flux can be expected with a thicker GDL.

3.2.3 Thickness effect on ohmic resistance

Apart from gas transport, the electron conduction between the catalyst layer and BP is also affected by the thickness and porosity of GDL. The ohmic resistance of the GDL can be determined by equation (31):

$$R = \rho \bullet \frac{L}{S} \tag{31}$$

where ρ represents the resistivity, L represents the length of conductor, S represents the cross-

sectional area, and this equation can be modified as equation (32):

$$R = \rho \bullet \frac{\delta_{GDL}}{S} \tag{32}$$

Thus, the variation of ohmic resistance with different anode and cathode GDL thicknesses are drawn as blue curves in Fig. 6. Since the anode and cathode share the same structure, the same value of ohmic resistance can be obtained with the same value of thickness. To conclude, a thicker GDL would result in a larger ohmic resistance.

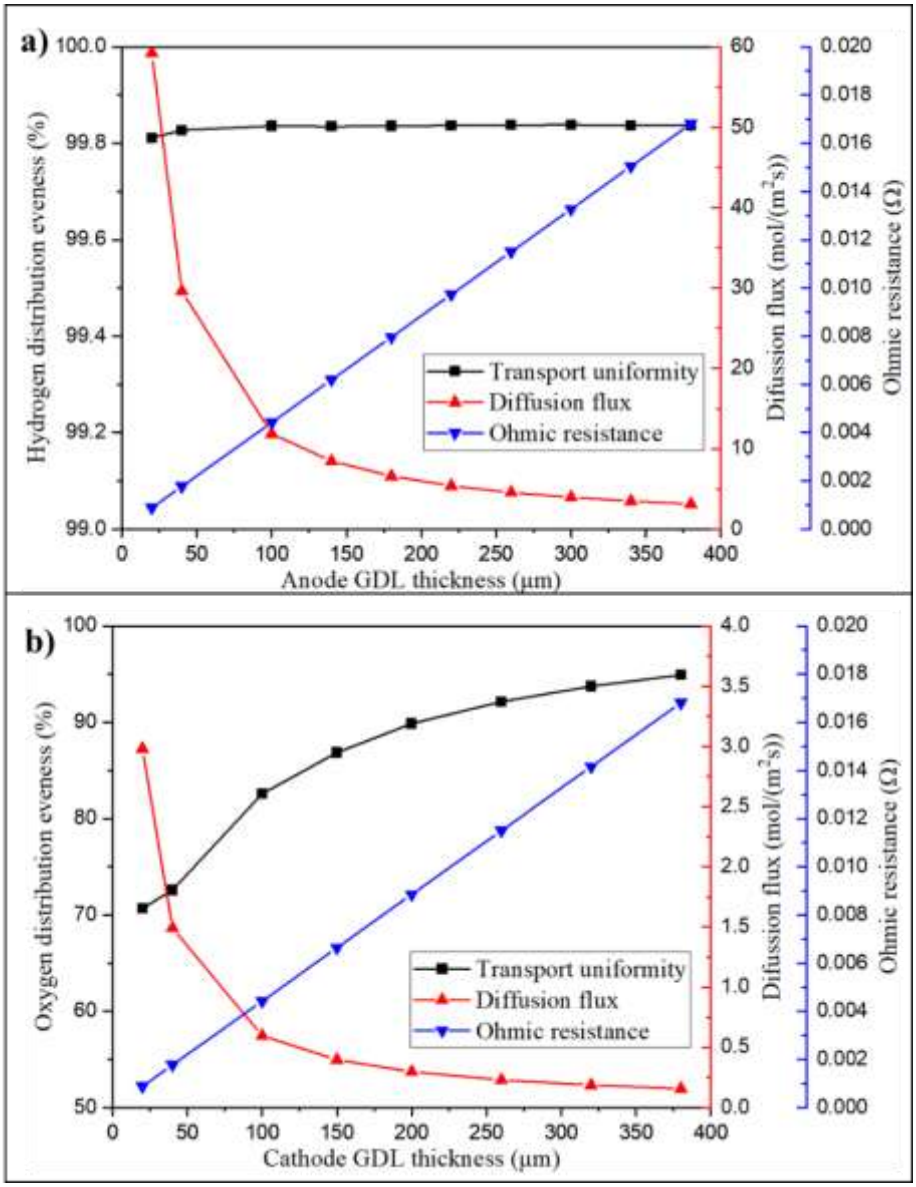

Fig. 6. Effect of GDL thickness on flow uniformity, diffusion flux and ohmic resistance

3.2.4 Thickness effect on cell performance

Fig. 7 shows the variation of current density at 0.4 V with different anode and cathode GDL thicknesses. At the anode, a slight increase of current density was observed with anode GDL thickness increasing from 20 μm to 100 μm. This can be attributed by the slight increment of hydrogen flow uniformity in Fig. 6(a). In this thickness range, as the diffusion resistance and ohmic loss are both low, the cell performance was improved consequently. When the thickness of anode GDL is further increased to be higher than 100 μm, the cell performance is found to decrease gradually, which is caused by a higher ohmic loss and lower diffusion flux (higher diffusion resistance). As a result, an optimal anode GDL thickness of about 100 μm is observed.

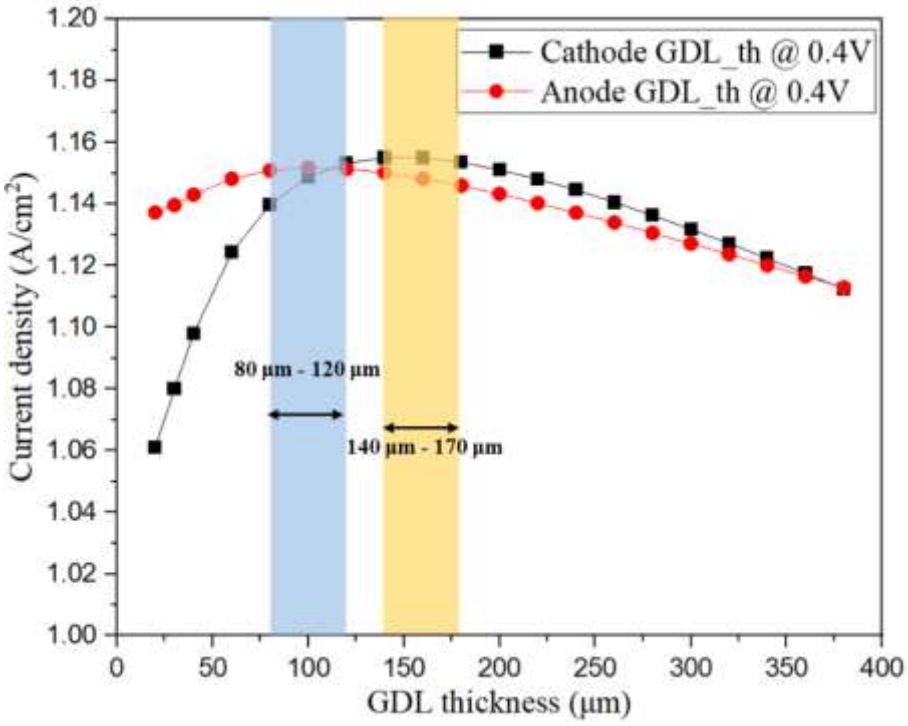

Fig. 7. Current density at 0.4 V with different GDLs' thicknesses

At the cathode, the cell performance is more significantly increased with increasing cathode GDL thickness from about 20 μm to 150 μm. This can be attributed by the more obvious increment of oxygen flow uniformity in Fig. 6(b) from 70% to 86% when the cathode

GDL thickness increases from 20 μm to 150 μm, which significantly improves the performance of the cell under the rib, leading to higher average cell performance. Similar to the anode, the cell performance is found to decrease with further increase in cathode GDL thickness beyond 150 μm. Consequently, an optimal cathode GDL thickness of about 150 μm is found.

In LT-PEMFC, it is reported that the GDL could improve the distribution uniformity of reactants [37], leading to enhanced overall cell performance. However, a too thick GDL could cause a high concentration loss, leading to performance reduction. For example, Chun et al. [38] reported lower cell performance with GDL thickness of 380 μm than that with GDL thickness of 200 μm. This study indicates the existence of optimal GDL thickness for LT-PEMFC as well. A more comprehensive study on the thickness of GDL in LT-PEMFC is needed.

Based on the discussion above and considering the practical fabrication of GDL, it can be concluded that the optimal ranges for anode and cathode GDL thickness would be 80 - 120 μm and 140 – 170 μm respectively (see Fig. 7) in order to achieve higher cell performance. To quantify the performance improvement, a comparison of the cell performance at different working voltages with different optimization strategies are given in Table 5. The values in second column represents the current density with both anode and cathode GDL thickness to be 380 μm. Third column shows the current density and performance increment at different working voltages after the optimization of anode GDL. Fourth and fifth column shows the similar results after optimization of cathode GDL and both two GDLs.

It can be seen that a larger value of performance increment is observed with a lower working voltage which can be regarded as higher electrical loading as well. With the optimization of anode GDL thickness, a 3.5% increment of current density at 0.4 V can be

achieved. By optimizing the cathode GDL thickness, the cell performance can be increased by 3.8%. After optimization of both anode and cathode GDL thickness, the cell performance can be improved by 7.7%, in comparison with the base case.

Table 5 Current density and performance increment under different voltages with optimization of the GDLa and GDLc thicknesses

Voltage (V)	Data in validation (A/cm^2)	Optimization of GDLa (A/cm^2)	Optimization of GDLc (A/cm^2)	Optimization of both GDLs (A/cm^2)
0.8	0.02817	0.02833	0.02819	0.02834
0.7	0.15798	0.16089	0.15938	0.16249
0.6	0.40972	0.42110	0.41822	0.43070
0.5	0.73838	0.76304	0.76107	0.78862
0.4	1.1127	1.1518	1.1552	1.1982
0.8	/	0.6%	0.1%	0.6%
0.7	/	1.8%	0.9%	2.9%
0.6	/	2.8%	2.1%	5.1%
0.5	/	3.3%	3.1%	6.8%
0.4	/	3.5%	3.8%	7.7%

3.3 Effect of GDLs' porosity

3.3.1 Porosity effect on cell performance

Porosity is another key controllable parameter which would significantly affects the electrical, thermal, and transport properties of GDL, therefore affecting cell performance. Recently, Jha et al. [31] concluded that the optimal porosity should be 50% - 60% based on their study in a porosity range of 20% to 60%. A similar research was conducted and the results of current densities at 0.4 V are shown as black line in Fig. 8(a) with a total range of porosity from 0 to 100%. In this case, it can be seen that 100% porosity would be optimal as the cell performance continue to increase with increasing GDL porosity.

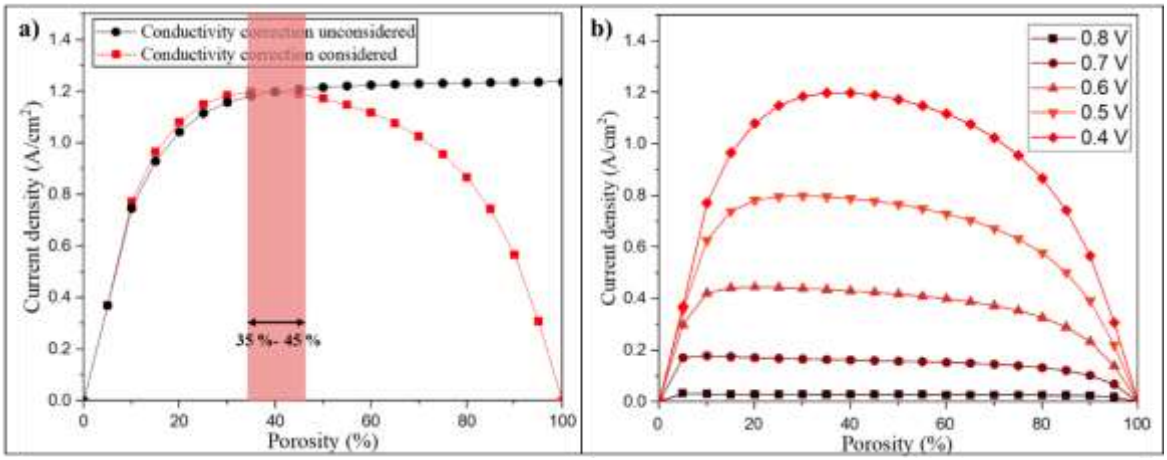

Fig. 8. (a) Current density at 0.4 V with different GDLs' porosities with and without conductivity correction. (b) Current density with different GDLs' porosities at different voltages after consideration of conductivity correction

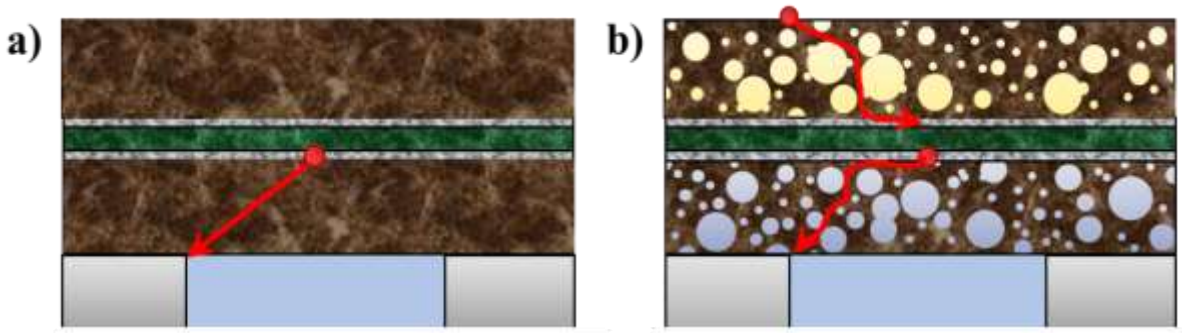

Fig. 9. Schematic of porosity effect on electron transfer with (a) solid GDL (b) normal GDL

However, as discussed in the introduction section, the porosity effect on electrical conductivity was neglected in their work, which was incorrect as electron conduction should be affected by the GDL porosity and 100% porosity would not allow electron conduction. For better understanding, electron conduction through GDL with 0% porosity (Fig. 9a) and representative 40% porosity (Fig. 9b) was illustrated in Fig. 9. With 0% porosity, the electrons should transport through the GDL as straight line (Fig. 9a). For comparison, the path for electron conduction becomes tortuous when the GDL porosity is 40%, due to the existence of pores (Fig. 9b). Thus, the electrical conductivity of GDL should consider the porosity effect, which can be determined by Brugman equation (33):

$$\sigma_{\text{eff}} = (1-\varepsilon)^{1.5} \bullet \sigma_0 \qquad (33)$$

Obviously, the effect of GDL porosity on electron conduction is significant as both anode and cathode GDLs are porous. After fully considering the effect of GDL porosity on electron conduction, a completely new curve can be obtained as red line in Fig. 8(a), which clearly shows that the current density should be 0 with GDL porosity 0% or 100%. This is because when porosity is 0, no gaseous reactants can be transferred to the reaction sites through the GDL while 100% porosity means empty GDL and no solid phase for electron conduction. Thus, the whole fuel cell would be open circuit with a 100% GDL porosity. Moreover, the current densities under different working voltages are examined as shown in Fig. 8(b). The five curves all share the similar trend. Based on this new result, it can be concluded that the optimal porosity of GDL should be 35% - 45% which brings a best cell performance and covers a large range of working voltage.

3.3.2 Porosity effect on flow uniformity

To deeply reveal the mechanism of how porosity affects the cell performance, similar analysis as described in section 3.2 was conducted. Since the effect on oxygen transport is much more significant than hydrogen transport, only the cathode results were given as shown in Fig. 10. It can be seen that increasing the cathode GDL porosity from 10% to 90% not only improves the flow uniformity from 54.85% to 98.04% but also increase the oxygen concentration. When the porosity was 10%, only the cell area under the channel had a relatively high concentration while the oxygen concentration in the area under the rib rather low, which would result in rather poor cell performance under the rib. With increasing GDL porosity, the oxygen concentration in the area under the rib can be improved, which in turn can increase the average performance of the entire cell. The variation of oxygen flow uniformity with different

porosity is drawn with black line in Fig. 11.

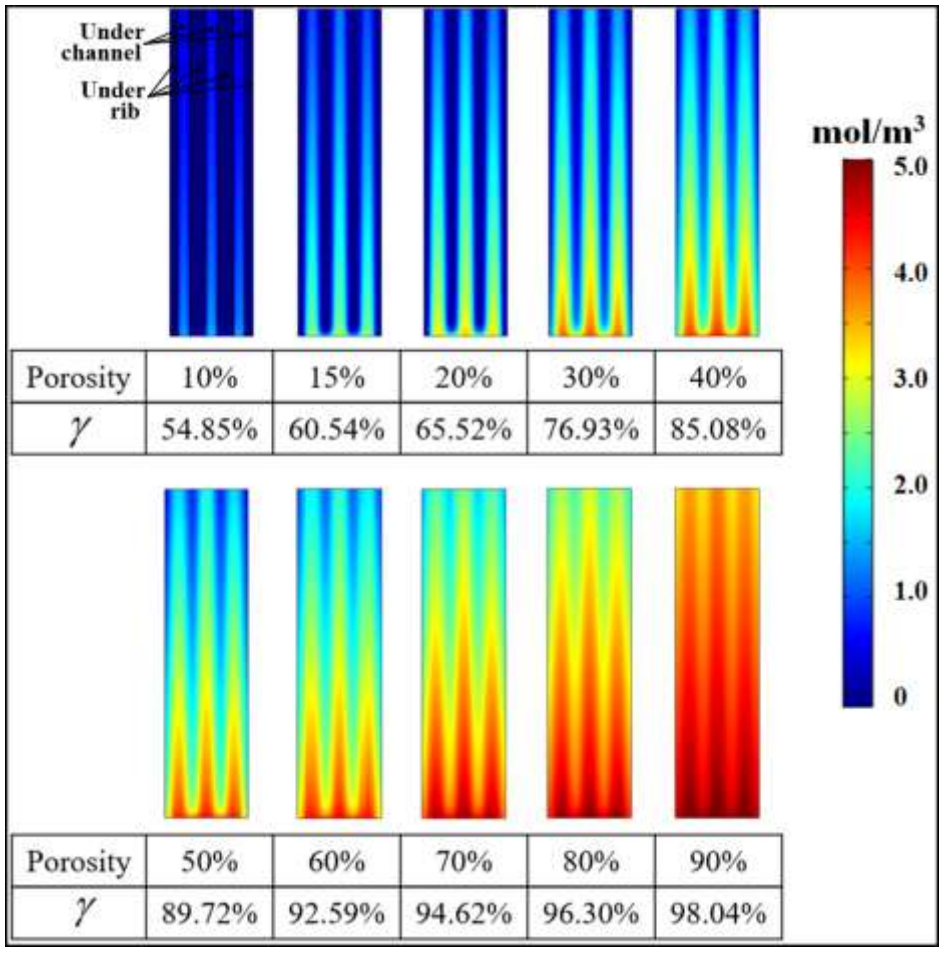

Porosity	10%	15%	20%	30%	40%
γ	54.85%	60.54%	65.52%	76.93%	85.08%

Porosity	50%	60%	70%	80%	90%
γ	89.72%	92.59%	94.62%	96.30%	98.04%

Fig. 10. Oxygen concentration distribution in the catalyst layer with different porosity

3.3.3 Porosity effect on diffusion flux

In section 3.2.3, the adjusted equation (30) reveals the relationship between the GDL thickness and diffusion flux. In that case, the diffusion coefficient is a constant since the variation of thickness would not change the structure of GDL. However, when the GDL porosity is changed, both the electron conduction pathway and the gas transport are affected. Thus, the diffusion coefficient should consider the porosity effect and determined by equation (34):

$$D_{\text{eff}} = \frac{\varepsilon}{\tau} D_0 \quad , \quad \tau = \varepsilon^{-1/2} \tag{34}$$

where τ represents the tortuosity. Thus, the equation (30) can be adjusted to be porosity-dependent according to equation (35):

$$J = \frac{\varepsilon}{\tau} D_0 \bullet \frac{C_{\text{channel}} - C_{CL}}{\delta_{GDL}} \tag{35}$$

Therefore, the red curve showing the relationship between the diffusion flux and porosity can be achieved and drawn in Fig. 11. The results shows that the diffusion flux has a positive correlation with GDLs' porosity.

3.3.4 Porosity effect on ohmic resistance

In section 3.2.3, the adjusted equation (32) reveals the relationship between the GDL thickness and ohmic resistance. In that case, the resistivity is a constant since the variation of thickness would not change this property. However, as illustrated in Fig. 9, the conductivity needs correction as shown in equation (33). In addition, a very important relationship should be applied as equation (36):

$$\rho = \frac{1}{\sigma} \tag{36}$$

Combined with equation (33 & 36), equation (32) could be transformed into equation (37):

$$R = \frac{1}{(1-\varepsilon)^{1.5} \bullet \sigma_0} \bullet \frac{\delta_{GDL}}{S} \tag{37}$$

which indicates how the porosity affects the ohmic resistance. Since the porosity directly affects the GDLs' electron conductivity, the effective conductivity with different porosity was drawn as blue line in Fig. 11. The result shows that a higher porosity would greatly decrease the effective electron conductivity, thus leading to a larger ohmic resistance according to equation (37).

3.3.5 Further discussion

After the comprehensive investigation of porosity effect on flow uniformity, diffusion flux and effective conductivity, a deeper understanding of porosity effect on cell performance can be achieved. Firstly, there would be no current density when porosity is 0 because the diffusion flux is 0, which means no reactant can be transported to CL and no reaction happens. As shown in Fig. 11, when the porosity increases from 0 to 40%, a significant performance improvement is observed (see Fig. 8(a)) due to the great increment of both flow uniformity and diffusion flux (see Fig .11 (black line & red line)). Similar phenomenon was reported by Chun et al. [38] that the gas permeability of GDL increases when the porosity increases according to their experimental results on LT-PEMFC. However, the increase in porosity would decrease the effective electronic conductivity of GDL, especially at a high porosity.

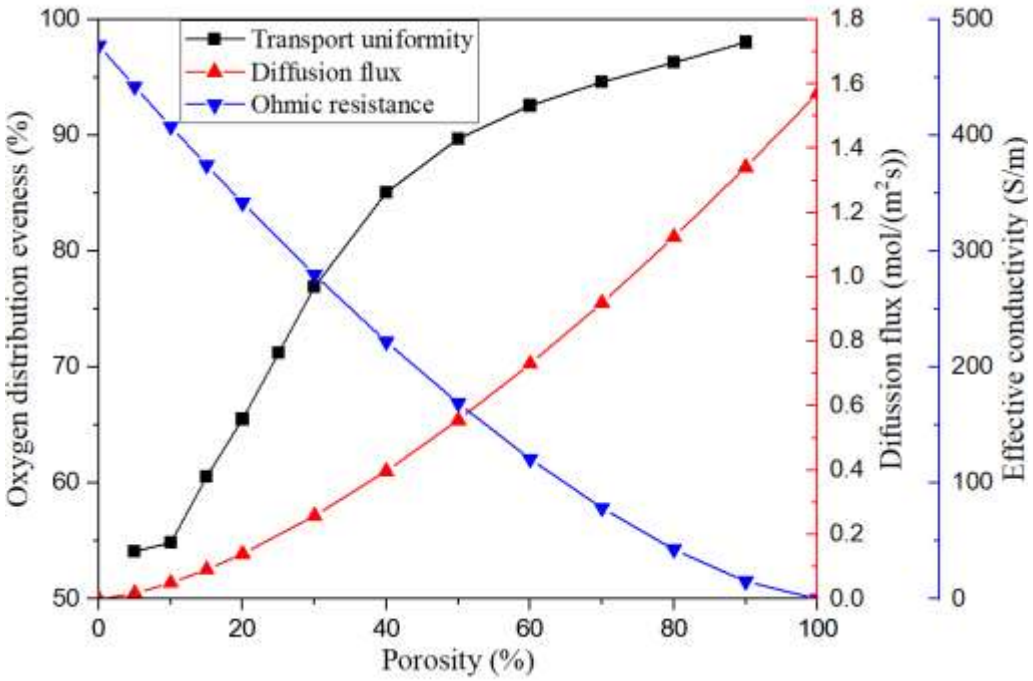

Fig. 11. Effect of GDL porosity on flow uniformity, diffusion flux and effective conductivity

When the porosity reaches 100%, the electron conductivity is decreased to 0, leading to zero current density and thus open-circuit condition for the cell. The porosity effect on the electrical conductivity was confirmed by Inoue et al. [39]. Based on their experimental results,

it is reported that the GDL with increasing porosity would have a decrement in electrical conductivity.

As mentioned above, the optimal porosity would be 35% - 45% based on the comprehensive effect of porosity on cell performance. The maximum value of current density can be achieved at a porosity of 40%, which happens to be the usually used GDL porosity in the literature. However, this study illuminates the effects of GDL porosity on HT-PEMFC performance.

4. Conclusion

In this work, a numerical non-isothermal three-channels 3D model was developed to investigate the effect of GDLs' properties on cell performance. The thickness and porosity were selected for optimization. Unlike previous modeling studies on the cell performance with different parameters, the comprehensive study thoroughly examined the effects of the thickness and porosity on flow uniformity, diffusion flux and ohmic resistance. Consequently, a fundamental understanding on the thickness and porosity effects is obtained for design optimization.

It was found that the GDL can help improve the reactants distribution uniformity inside the CL, especially at cathode side. When the thickness was increased from 20 μm, performance improvement was observed due to the increasing reactants flow uniformity, which improved the oxygen concentration for cell area under the rib, leading to enhanced average performance of the entire cell. However, when the GDL thickness was further increased, the decline of diffusion flux and increasing ohmic resistance becomes more significant, leading to a lower cell performance. It is also found that increasing GDL porosity increases both flow uniformity

and diffusion flux, therefore improving the performance. However, the effective electron conductivity is found to decrease with increasing GDL porosity. Since the cell performance depends on the combined effects of these three factors, the current density would decrease with the further increasing porosity. Based on the results and discussions above, the optimal thickness for anode and cathode GDL would be 80-120 μm and 140-170 μm, respectively. The optimal value for GDL porosity ranges from 35% to 45%.

After optimization of both GDLs' thickness and porosity, a total performance increment 7.7% of cell performance was achieved. Future work should be conducted to experimentally realize the optimized GDL design. It should be noted that in the practical application, the compression during the fuel cell assembly would affect both the local porosity and thickness of GDL. Besides, the GDL under the rib would be compressed more than the GDL under the channel, which would make the mass transport under the rib more difficult. This factor should be considered in the further study.

Appendix

The detailed calculation of reactants distribution uniformity, diffusion flux and ohmic resistance are discussed in this section.

Appendix A Calculation of reactants distribution uniformity

The reactants distribution uniformity is governed by the equation (38).

$$\gamma = 1 - \frac{1}{2n} \sum_{n=1}^{n} \frac{\sqrt{(c_n - \bar{c})^2}}{\bar{c}} \tag{38}$$

where c represents the concentration value, n represents the point n, $\bar{c}$ represents the average value of concentration. Therefore, in the case of the same X axis position, the reactants

distribution uniformity at the specific X position can be achieved. In this case, the $\bar{c}$ represents linear average value of concentration in Y axis. When adopting different X axis positions, the correspondent reactants distribution uniformity could be calculated and Fig. 5 was drawn. The value of reactants distribution uniformity in the whole cross-sectional CL is also achieved similarly, in which case the $\bar{c}$ represents the average value of whole plane. Therefore, the reactants distribution uniformity with different GDL design can be obtained and black curves in Fig. 6 & Fig. 11 were drawn.

Appendix B Calculation of diffusion flux

In section 3.2.2, the calculation of diffusion flux is governed by the equation (39) with different thicknesses of GDL.

$$J = D\frac{C_{\text{channel}} - C_{CL}}{\delta_{GDL}} \tag{39}$$

where C_{channel} and C_{CL} represent the concentration value in the channel and catalyst layer respectively. The diffusion coefficient D is calculated by the function listed in Table 1. Thus, the red curves in Fig. 6 were drawn.

In section 3.3.3, when investigating the effect of GDL porosity on diffusion flux, it should be noted that the diffusion coefficient would be affected. Thus, the correction of diffusion coefficient is adopted as shown in equation (40):

$$J = \frac{\varepsilon}{\tau} D_0 \bullet \frac{C_{\text{channel}} - C_{CL}}{\delta_{GDL}} \tag{40}$$

where ε represents the porosity and τ represents the tortuosity which is governed by equation (34). Thus, the red curve in Fig. 11 was drawn.

Appendix C Calculation of ohmic resistance and effective conductivity

In section 3.2.3, the calculation of ohmic resistance is governed by the equation (41) with different thicknesses of GDL.

$$R = \rho \bullet \frac{\delta_{GDL}}{S} \tag{41}$$

where ρ represents the resistivity of the material and equals to the reciprocal value of conductivity. Therefore, the blue curves in Fig. 6 can be directly drawn.

In section 3.3.3, the calculation of ohmic resistance would be different because the porosity would affect the conductivity. Thus, the correction of effective conductivity should be added as shown in equation (42).

$$\sigma_{\text{eff}} = (1-\varepsilon)^{1.5} \bullet \sigma_0 \tag{42}$$

Then, different ohmic resistance with different designs of GDL can be obtained with equation (43).

$$R = \frac{1}{(1-\varepsilon)^{1.5} \bullet \sigma_0} \bullet \frac{\delta_{GDL}}{S} \tag{43}$$

Because the porosity affects the conductivity first, thus the curve representing the effective conductivity was drawn in Fig. 11.

Acknowledgement

M. Ni thanks the funding support (Project Number: PolyU 152064/18E) from Research Grant Council, University Grants Committee, Hong Kong SAR.

Reference

[1] Y Wang, B Seo, B Wang, N Zamel, K Jiao, XC Adroher, Fundamentals, materials, and machine learning of polymer electrolyte membrane fuel cell technology, Energy and AI, 1(2020)100014.

[2] E. Jannelli, M. Minutillo, A. Perna, Analyzing microcogeneration systems based on LT-PEMFC and HT-PEMFC by energy balances, Applied Energy, 108 (2013) 82-91.

[3] B Wang, G Zhang, H Wang, J Xuan, K Jiao, Multi-physics-resolved digital twin of proton exchange membrane fuel cells with a data-driven surrogate model, Energy and AI, 1(2020) 100004.

[4] N. Zamel, X. Li, Transient analysis of carbon monoxide poisoning and oxygen bleeding in a PEM fuel cell anode catalyst layer, International Journal of Hydrogen Energy, 33(4) (2008) 1335-1344.

[5] Q. Li, R. He, J.-A. Gao, J.O. Jensen, N.J. Bjerrum, The CO poisoning effect in PEMFCs operational at temperatures up to 200 C, Journal of the Electrochemical Society, 150(12) (2003) A1599.
[6] A. Brouzgou, A. Seretis, S. Song, P.K. Shen, P. Tsiakaras, CO tolerance and durability study of PtMe (Me= Ir or Pd) electrocatalysts for H2-PEMFC application, International Journal of Hydrogen Energy, (2020).
[7] Y. Ferng, A. Su, J. Hou, Parametric investigation to enhance the performance of a PBI-based high-temperature PEMFC, Energy conversion and management, 78 (2014) 431-437.
[8] A. Bergmann, D. Gerteisen, T. Kurz, Modelling of CO poisoning and its dynamics in HTPEM fuel cells, Fuel Cells, 10(2) (2010) 278-287.
[9] M. Boaventura, H. Sander, K.A. Friedrich, A. Mendes, The influence of CO on the current density distribution of high temperature polymer electrolyte membrane fuel cells, Electrochimica Acta, 56(25) (2011) 9467-9475.
[10] J. Zhang, Y. Xiang, S. Lu, S.P. Jiang, High temperature polymer electrolyte membrane fuel cells for integrated fuel cell–methanol reformer power systems: a critical review, Advanced Sustainable Systems, 2(8-9) (2018) 1700184.
[11] S.J. Andreasen, J.R. Vang, S.K. Kær, High temperature PEM fuel cell performance characterisation with CO and CO2 using electrochemical impedance spectroscopy, International journal of hydrogen energy, 36(16) (2011) 9815-9830.
[12] J.A. Asensio, E.M. Sánchez, P. Gómez-Romero, Proton-conducting membranes based on benzimidazole polymers for high-temperature PEM fuel cells. A chemical quest, Chemical Society Reviews, 39(8) (2010) 3210-3239.
[13] G. Lakshminarayana, M. Nogami, I. Kityk, Synthesis and characterization of anhydrous proton conducting inorganic–organic composite membranes for medium temperature proton exchange membrane fuel cells (PEMFCs), Energy, 35(12) (2010) 5260-5268.
[14] H.-L. Lin, T.L. Yu, W.-K. Chang, C.-P. Cheng, C.-R. Hu, G.-B. Jung, Preparation of a low proton resistance PBI/PTFE composite membrane, Journal of power sources, 164(2) (2007) 481-487.
[15] Z. Liu, J.S. Wainright, M.H. Litt, R.F. Savinell, Study of the oxygen reduction reaction (ORR) at Pt interfaced with phosphoric acid doped polybenzimidazole at elevated temperature and low relative humidity, Electrochimica Acta, 51(19) (2006) 3914-3923.
[16] Y. Zhai, H. Zhang, D. Xing, Z.-G. Shao, The stability of Pt/C catalyst in H3PO4/PBI PEMFC during high temperature life test, Journal of Power Sources, 164(1) (2007) 126-133.
[17] M. Prokop, R. Kodym, T. Bystron, M. Drakselova, M. Paidar, K. Bouzek, Degradation kinetics of Pt during high-temperature PEM fuel cell operation part II: Dissolution kinetics of Pt incorporated in a catalyst layer of a gas-diffusion electrode, Electrochimica Acta, 333 (2020) 135509.
[18] X. Li, I. Sabir, Review of bipolar plates in PEM fuel cells: Flow-field designs, International journal of hydrogen energy, 30(4) (2005) 359-371.
[19] X.-D. Wang, Y.-Y. Duan, W.-M. Yan, Numerical study of cell performance and local transport phenomena in PEM fuel cells with various flow channel area ratios, Journal of Power Sources, 172(1) (2007) 265-277.
[20] Y. Kerkoub, A. Benzaoui, F. Haddad, Y.K. Ziari, Channel to rib width ratio influence with various flow field designs on performance of PEM fuel cell, Energy Conversion and Management, 174 (2018) 260-275.
[21] Z. Niu, Y. Wang, K. Jiao, J. Wu, Two-phase flow dynamics in the gas diffusion layer of proton exchange membrane fuel cells: volume of fluid modeling and comparison with experiment, Journal of The Electrochemical Society, 165(9) (2018) F613.
[22] Y. Wang, C.-Y. Wang, A nonisothermal, two-phase model for polymer electrolyte fuel cells, Journal of

the electrochemical society, 153(6) (2006) A1193.
[23] J.T. Gostick, M.A. Ioannidis, M.D. Pritzker, M.W. Fowler, Impact of liquid water on reactant mass transfer in PEM fuel cell electrodes, Journal of the Electrochemical Society, 157(4) (2010) B563.
[24] J. Benner, M. Mortazavi, A.D. Santamaria, Numerical simulation of droplet emergence and growth from gas diffusion layers (GDLs) in proton exchange membrane (PEM) fuel cell flow channels, in: ASME International Mechanical Engineering Congress and Exposition, American Society of Mechanical Engineers, 2018, pp. V06AT08A065.
[25] Y. Wang, D.F.R. Diaz, K.S. Chen, Z. Wang, X.C. Adroher, Materials, technological status, and fundamentals of PEM fuel cells–a review, Materials today, 32 (2020) 178-203.
[26] Gas diffusion layer (GDL) comparison Chart n.d.. https://fuelcellsetc.com/helpful-tools/gas-diffusion-layer-gdlcomparison-chart/(accessed Feburary 8, 2021). in.
[27] A. El-Kharouf, T.J. Mason, D.J. Brett, B.G. Pollet, Ex-situ characterisation of gas diffusion layers for proton exchange membrane fuel cells, Journal of Power sources, 218 (2012) 393-404.
[28] Q. Chen, Z. Niu, H. Li, K. Jiao, Y. Wang, Recent progress of gas diffusion layer in proton exchange membrane fuel cell: Two-phase flow and material properties, International Journal of Hydrogen Energy, (2021).
[29] Z. Zhang, P. He, Y.-J. Dai, P.-H. Jin, W.-Q. Tao, Study of the mechanical behavior of paper-type GDL in PEMFC based on microstructure morphology, International Journal of Hydrogen Energy, 45(53) (2020) 29379-29394.
[30] T.J. Jaber, R. Jaralla, M.A. Sulaiman, K. Bourouni, Numerical Study on High Temperature PEM Fuel Cell (HTPEMFC), in: ICTEA: International Conference on Thermal Engineering, 2017.
[31] V. Jha, R. Hariharan, B. Krishnamurthy, A 3 dimensional numerical model to study the effect of GDL porosity on high temperature PEM fuel cells, International Journal of Heat and Mass Transfer, 161 (2020) 120311.
[32] S. Li, B. Sundén, Three-dimensional modeling and investigation of high temperature proton exchange membrane fuel cells with metal foams as flow distributor, International Journal of Hydrogen Energy, 42(44) (2017) 27323-27333.
[33] A.K. Coker, Appendix C: Physical properties of liquids and gases, Ludwig's Applied Process Design for Chemical and Petrochemical Plants, 1 (2007) 827-862.
[34] M.W. Chase Jr, NIST-JANAF thermochemical tables, J. Phys. Chem. Ref. Data, Monograph, 9 (1998).
[35] E. Ubong, Z. Shi, X. Wang, Three-dimensional modeling and experimental study of a high temperature PBI-based PEM fuel cell, Journal of The Electrochemical Society, 156(10) (2009) B1276.
[36] H. Weltens, H. Bressler, F. Terres, H. Neumaier, D. Rammoser, Optimisation of catalytic converter gas flow distribution by CFD prediction, 0148-7191, SAE Technical Paper, 1993.
[37] R. Omrani, B. Shabani, Gas diffusion layer modifications and treatments for improving the performance of proton exchange membrane fuel cells and electrolysers: A review, International Journal of Hydrogen Energy, 42(47) (2017) 28515-28536.
[38] J.H. Chun, K.T. Park, D.H. Jo, S.G. Kim, S.H. Kim, Numerical modeling and experimental study of the influence of GDL properties on performance in a PEMFC, International Journal of Hydrogen Energy, 36(2) (2011) 1837-1845.
[39] G. Inoue, K. Yokoyama, J. Ooyama, T. Terao, T. Tokunaga, N. Kubo, M. Kawase, Theoretical examination of effective oxygen diffusion coefficient and electrical conductivity of polymer electrolyte fuel cell porous components, Journal of Power Sources, 327 (2016) 610-621.